

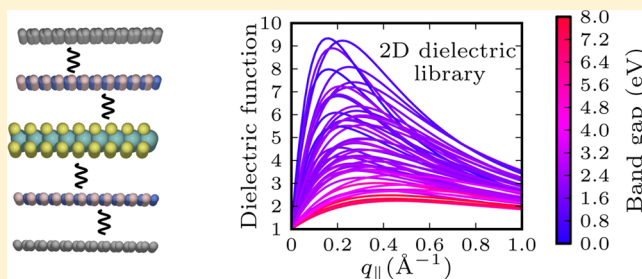
Dielectric Genome of van der Waals Heterostructures

Kirsten Andersen,^{*,†} Simone Latini,^{†,‡} and Kristian S. Thygesen^{*,†,‡}[†]Center for Atomic-scale Materials Design, Department of Physics, and [‡]Center for Nanostructured Graphene, Technical University of Denmark, DK-2800 Kgs. Lyngby, Denmark

S Supporting Information

ABSTRACT: Vertical stacking of two-dimensional (2D) crystals, such as graphene and hexagonal boron nitride, has recently lead to a new class of materials known as van der Waals heterostructures (vdWHs) with unique and highly tunable electronic properties. Ab initio calculations should in principle provide a powerful tool for modeling and guiding the design of vdWHs, but in their traditional form such calculations are only feasible for commensurable structures with a few layers. Here we show that the dielectric properties of realistic, incommensurable vdWHs comprising hundreds of layers can be efficiently calculated using a multiscale approach where the dielectric functions of the individual layers (the dielectric building blocks) are computed ab initio and coupled together via the long-range Coulomb interaction. We use the method to illustrate the 2D–3D transition of the dielectric function of multilayer MoS₂ crystals, the hybridization of quantum plasmons in thick graphene/hBN heterostructures, and to demonstrate the intricate effect of substrate screening on the non-Rydberg exciton series in supported WS₂. The dielectric building blocks for a variety of 2D crystals are available in an open database together with the software for solving the coupled electrodynamic equations.

KEYWORDS: van der Waals heterostructures, 2D materials, density functional theory, dielectric function, excitons, plasmons



The class of 2D materials, which started with graphene, is rapidly expanding and now includes metallic and semiconducting transition metal dichalcogenides¹ in addition to group III–V semimetals, semiconductors, and insulators.² These atomically thin materials exhibit unique optoelectronic properties with high technological potential.^{3–7} However, the 2D materials only form the basis of a new and much larger class of materials consisting of vertically stacked 2D crystals held together by weak van der Waals forces. In contrast to conventional heterostructures that require complex and expensive crystal-growth techniques to epitaxially grow the single-crystalline semiconductor layers, van der Waals heterostructures (vdWHs) can be stacked in ambient conditions with no requirements of lattice matching. The latter implies a weaker constraint, if any, on the choice of materials that can be combined into vdWHs.

The weak interlayer binding suggests that the individual layers of a vdWH largely preserve their original 2D properties modified only by the long-range Coulomb interaction with the surrounding layers. Turning this argument around, it should be possible to predict the overall properties of a vdWH from the properties of the individual layers. In this Letter we show that this can indeed be achieved for the dielectric properties. Conceptually, this extends the Lego brick picture used by Geim and Grigorieva⁸ for the atomic structure of a vdWH, to its dielectric properties. Specifically, we develop a semiclassical model that takes as input the dielectric functions of the individual isolated layers computed fully quantum mechanically and condensed into the simplest possible representation, and

couples them together via the Coulomb interaction, see Figure 1. Despite the complete neglect of interlayer hybridization, the model provides an excellent account of both the spatial and dynamical dielectric properties of vdWHs. The condensed representation of the dielectric functions of the 2D crystals can thus be regarded as the dielectric genome of the vdWH.

In addition to its conceptual value, our approach overcomes a practical limitation of conventional first-principles methods. Such methods are not only computationally demanding, but also rely on periodic boundary conditions, which are incompatible with the incommensurable interfaces found in vdWHs. In fact, for many purposes, an in-plane lattice mismatch between neighboring 2D crystals is preferred because it reduces the interlayer coupling, and thus minimizes the risk of commensurate–incommensurate transitions,⁹ and formation of Moire patterns¹⁰ and associated band structure reconstructions,¹¹ which are typical for systems with similar lattice constants. This emphasizes the need for alternative approaches for modeling vdWHs.

The dielectric function is one of the most important material response functions. It determines the effective interaction between charged particles in the material, contains information about the collective oscillations of the electron gas (plasmons),¹² and enters as a fundamental ingredient in many-body calculations of, e.g., excitons and quasiparticle

Received: March 31, 2015

Revised: June 3, 2015

Published: June 5, 2015

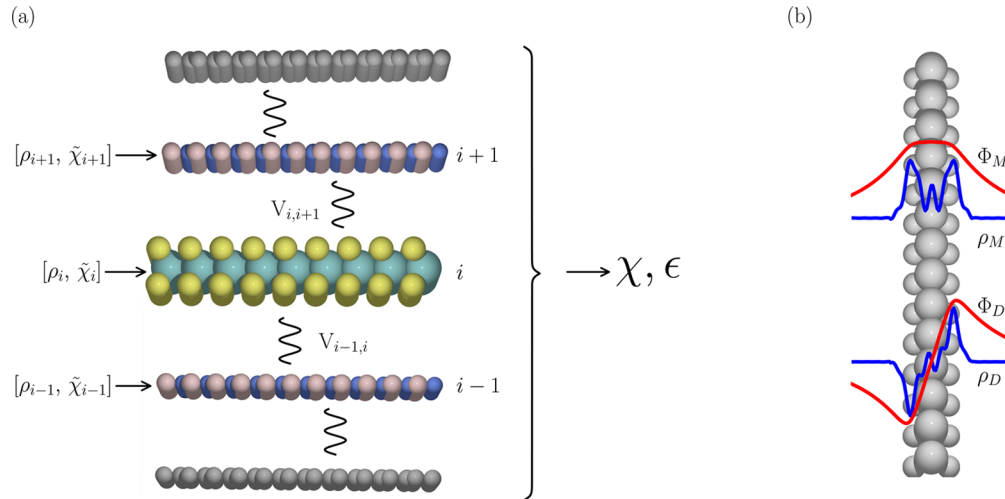


Figure 1. Schematic of the QEH model. (a) The density response function and dielectric function of the heterostructure are calculated from the dielectric building blocks of the individual layers assuming a purely electrostatic interaction between the layers. The dielectric building blocks are calculated ab initio for the isolated layers. They comprise the monopole and dipole components of the density response function, $\tilde{\chi}_{M/D}$, together with the spatial shape of the electron density, $\rho_{M/D}(z)$, induced by a constant and linear applied potential, respectively. (b) Monopole and dipole induced densities (blue) together with the associated potentials (red) for monolayer MoS₂.

band structures.^{13,14} We stress that in this work we consider only the electronic contributions to the dielectric properties. In particular, when referring to the static dielectric function we mean the dielectric function at frequencies smaller than any electronic transition energy but larger than the vibrational energies of the system.

The (inverse) dielectric function is related to the electron density response function, χ , via

$$\epsilon^{-1}(\mathbf{r}, \mathbf{r}', \omega) = \delta(\mathbf{r} - \mathbf{r}') + \int \frac{1}{|\mathbf{r} - \mathbf{r}''|} \chi(\mathbf{r}'', \mathbf{r}', \omega) d\mathbf{r}'' \quad (1)$$

In our quantum-electrostatic heterostructure (QEH) model the calculation of the dielectric function is divided into two parts. In the first part the in-plane averaged density response functions of the freestanding layers, $\chi_i(z, z', \mathbf{q}_{\parallel}, \omega)$, are obtained from ab initio calculations. In practice we treat the in-plane momentum transfer, \mathbf{q}_{\parallel} , as a scalar since most 2D materials are isotropic within the plane. From χ_i we calculate the magnitude of the monopole/dipole component of the density induced by a potential with a constant/linear variation across the layer and in-plane variation $\exp(i\mathbf{r}_{\parallel} \cdot \mathbf{q}_{\parallel})$

$$\tilde{\chi}_{i\alpha}(\mathbf{q}_{\parallel}, \omega) = \int z^{\alpha} \chi_i(z, z', \mathbf{q}_{\parallel}, \omega) z'^{\alpha} dz dz' \quad (2)$$

Here $\alpha = 0, 1$ for the monopole and dipole components, respectively. In addition we calculate the spatial form of the induced density, $\rho_{i\alpha}(z, \mathbf{q}_{\parallel})$. With a proper normalization of $\rho_{i\alpha}$ we can then write

$$\int \chi_i(z, z', \mathbf{q}_{\parallel}, \omega) z'^{\alpha} dz' = \tilde{\chi}_{i\alpha}(\mathbf{q}_{\parallel}, \omega) \rho_{i\alpha}(z, \mathbf{q}_{\parallel}) \quad (3)$$

We have found that while $\tilde{\chi}_{i\alpha}$ depends strongly on frequency, $\rho_{i\alpha}$ does not. The data set $(\tilde{\chi}_{i\alpha}, \rho_{i\alpha})$ with $\alpha = 0, 1$ or equivalently $\alpha = M, D$ constitutes the dielectric building block of layer i , as illustrated in Figure 1. According to eq 3 the dielectric building block allows us to obtain the density induced in the (isolated) layer i by a constant/linear potential. It is straightforward to extend the dielectric building blocks to account for higher-order moments in the induced density described by $\alpha > 1$, but we

have found the dipole approximation to be sufficient in all cases considered.

In the second part of the QEH model, the density response function of the vdWH in the discrete monopole/dipole representation is obtained by solving a Dyson-like equation that couples the dielectric building blocks together via the Coulomb interaction. The Dyson equation for the full density response function giving the magnitude of the monopole/dipole density on layer i induced by a constant/linear potential applied to layer j reads (omitting the \mathbf{q}_{\parallel} and ω variables for simplicity)

$$\chi_{i\alpha, j\beta} = \tilde{\chi}_{i\alpha} \delta_{i\alpha, j\beta} + \tilde{\chi}_{i\alpha} \sum_{k \neq i, \gamma} V_{i\alpha, k\gamma} \chi_{k\gamma, j\beta} \quad (4)$$

The Coulomb matrices are defined as

$$V_{i\alpha, k\gamma}(\mathbf{q}_{\parallel}) = \int \rho_{i\alpha}(z, \mathbf{q}_{\parallel}) \Phi_{k\gamma}(z, \mathbf{q}_{\parallel}) dz \quad (5)$$

where $\Phi_{k\gamma}$ is the potential associated with the induced density, $\rho_{k\gamma}$, which we calculate on a uniform grid by solving a 1D Poisson equation. Note that we leave out the self-interaction terms in eq 4 since the intralayer Coulomb interaction is already accounted for by the uncoupled $\tilde{\chi}_{i\alpha}$. The (inverse) dielectric function of eq 1 in the monopole/dipole basis becomes

$$\epsilon_{i\alpha, j\beta}^{-1}(\mathbf{q}_{\parallel}, \omega) = \delta_{i\alpha, j\beta} + \sum_{k\gamma} V_{i\alpha, k\gamma}(\mathbf{q}_{\parallel}) \chi_{k\gamma, j\beta}(\mathbf{q}_{\parallel}, \omega) \quad (6)$$

More details on the method and computations are provided in the Supporting Information.

A database containing the dielectric building blocks of a large collection of 2D materials has been constructed and is available from our Web site.¹⁵ It presently contains more than 50 transition metal dichalcogenides and oxides, graphene at different doping levels, and hBN, and more materials are being added. From here the data files can be downloaded together with a Python module for calculating the dielectric function and associated properties of any combination of these materials. QEH model calculations for vdWHs containing a few

hundred layers can be performed on a standard PC. To illustrate the variation in the dielectric properties of the 2D semiconductors, Figure 2 shows the q_{\parallel} -dependent static

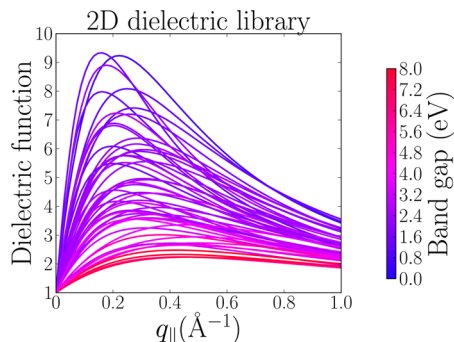


Figure 2. Static dielectric function $\epsilon(q_{\parallel}, \omega = 0)$ of the 51 transition metal dichalcogenides and oxides included in the database. As expected, the magnitude of the dielectric function is seen to correlate with the size of the band gap indicated by the color. The band gaps are calculated with G_0W_0 in ref 16.

dielectric functions of the monolayer transition metal dichalcogenides and -oxides presently contained in our database (for a complete overview of the materials see ref 16). All the dielectric functions show the same qualitative form, in particular they become 1 for $q_{\parallel} \rightarrow 0$ and $q_{\parallel} \rightarrow \infty$; however, there is quite some variation in their magnitude. As expected the size of the dielectric function correlates well with the size of the band gap of the material indicated by the color.

First-principles calculations were performed with the GPAW code.^{17,18} Single-particle wave functions and energies were calculated within the local density approximation (LDA) using 400 eV plane wave cutoff and at least 45×45 sampling of the 2D Brillouin zone. Density response functions and dielectric functions were calculated within the random phase approximation (RPA). The RPA does not include (direct) electron-hole interaction, but generally yields good results for the static dielectric properties of semiconductors and dynamical response of metals. Except for MoS_2 bulk, we included at least 15 Å of

vacuum in the super cells perpendicular to the layers and applied a truncated Coulomb kernel to avoid long-range screening between periodically repeated structures. All response functions were calculated in a plane wave basis including reciprocal lattice vectors up to at least 50 eV. A similar cut off was used for the sum over empty states, and convergence was carefully checked. The frequency dependence of the response functions was represented on a nonlinear frequency grid ranging from 0 to 35 eV, with an initial grid spacing of 0.02 eV. All details of the calculations and atomic structure geometries are provided in the Supporting Information.

As a first application of the QEH model, we study how the (static) dielectric function of a 2D material evolves as the layer thickness increases toward the bulk. One of the most characteristic differences between 2D and 3D materials is the behavior of the dielectric function in the long wavelength limit: For a bulk semiconductor, the dielectric function $\epsilon(q)$ tends smoothly to a value larger than unity as $q \rightarrow 0$. This is the static dielectric constant of the material, ϵ_{∞} . In contrast $\epsilon(q_{\parallel}) = 1 + O(q_{\parallel})$ for a 2D semiconductor implying a complete absence of screening in the long wavelength limit.^{19,20} Consequently, the concept of the dielectric constant does not exist for a freestanding 2D semiconductor.

Ab initio calculations were performed for the dielectric function of MoS_2 monolayer, bilayer, and bulk, and the QEH model was used for multilayer structures up to 100 layers. Figure 3b shows the dielectric functions averaged over the slabs, i.e., the macroscopic dielectric function, as a function of the in-plane momentum transfer. For large q_{\parallel} the dielectric functions show similar behavior. However, whereas $\epsilon(0) = 14$ for the bulk, the dielectric functions of the slabs decrease sharply to 1 for small q_{\parallel} . This demonstrates that the dielectric properties of a vdWH of thickness L are 2D like for $q_{\parallel} \ll 1/L$ and 3D like for $q_{\parallel} \gg 1/L$. Interestingly, also the result for bulk MoS_2 shows reminiscence of the 2D nature of the constituent layers, where the magnitude of the dielectric function has a slight drop when $q_{\parallel} \rightarrow 0$.

The QEH model describes the change in the dielectric function from mono- to bilayer very accurately in spite of the well-known differences between the mono- and bilayer band

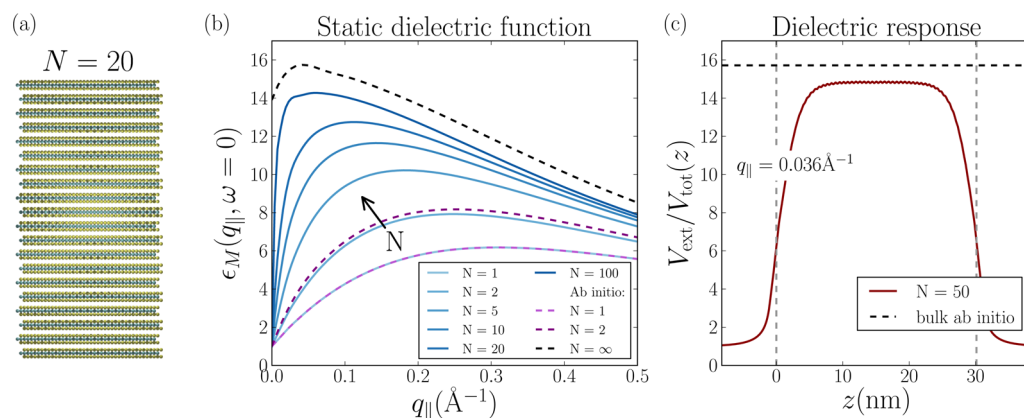


Figure 3. Two-dimensional to three-dimensional transition of the dielectric function. (a) Atomic structure of a 20 layer MoS_2 slab. (b) The macroscopic static dielectric function $\epsilon_M(q_{\parallel}, \omega = 0)$ as a function of the in-plane momentum transfer for different number of layers, N . The macroscopic dielectric function relates the total potential averaged over the width of the slab to an external potential of the form $V_{\text{ext}}(r_{\parallel}z) = \exp(ir_{\parallel} \cdot q_{\parallel})$. The dielectric functions increase monotonically with N converging slowly toward the dielectric function of bulk MoS_2 obtained from an ab initio calculation. Excellent agreement between the QEH model and the ab initio results are seen for $N = 1, 2$. The slow convergence toward the bulk result is due to the strong spatial variation of the induced potential in the surface region of the slabs. This can be seen in panel (c), which shows $V_{\text{ext}}/V_{\text{tot}}(z)$, i.e., the local dielectric function, for an external potential constant across the slab and with in-plane wave vector $q_{\parallel} = 0.036 \text{ Å}^{-1}$ for $N = 50$.

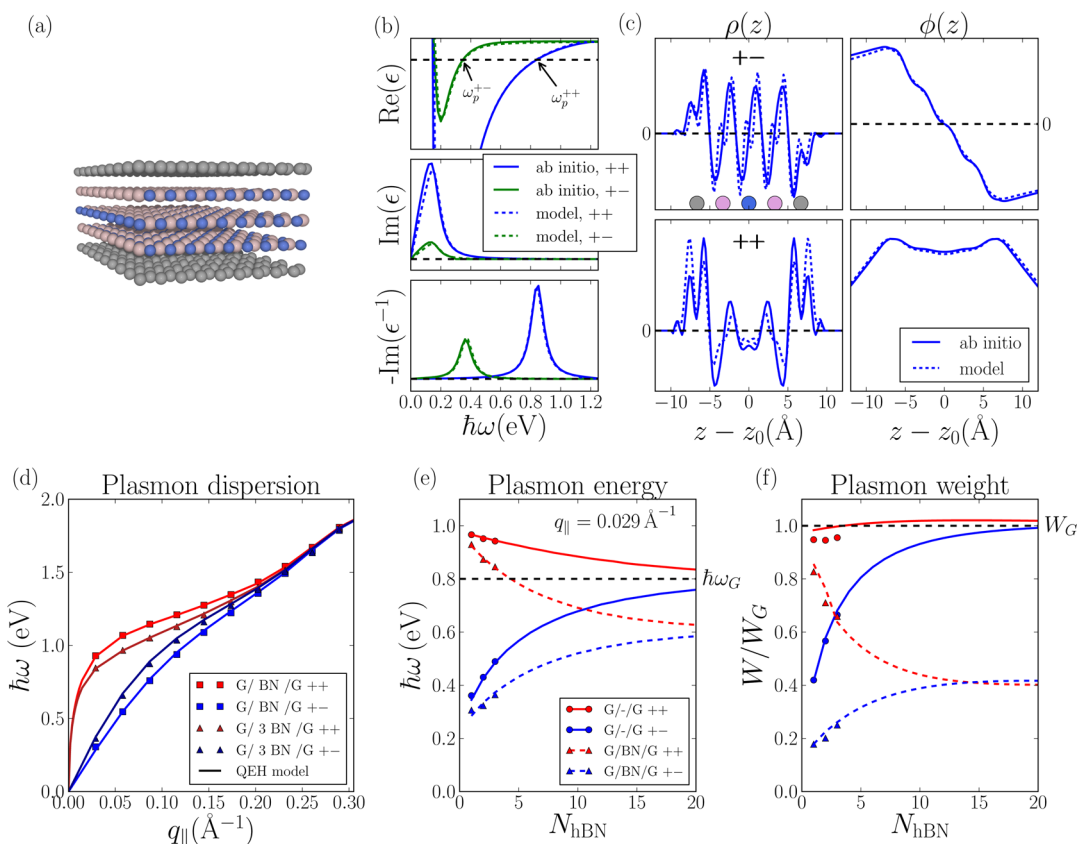


Figure 4. Plasmons in graphene/hBN heterostructures. (a) Two graphene sheets separated by three layers of hBN. (b) Eigenvalues of the heterostructure dielectric function $\epsilon(\omega)$. Only the two eigenvalue curves that fulfill the plasmon condition $\text{Re}\epsilon_n(\omega_p) = 0$ are shown. (c) The eigenpotential, $\psi(\omega_p)$, and associated density, $\rho(\omega_p)$, of the plasmon modes. The plasmons correspond to the antisymmetric (+-) and symmetric (++) combinations of the isolated graphene plasmons. (d) Plasmon dispersion for heterostructures containing 1 and 3 layers of hBN. Full lines denote the QEH model while ab initio results are denoted by symbols. (e,f) Energy and weight of the plasmon modes for up to 20 layers hBN between the graphene sheets. Results for equivalent structures with vacuum filling the gap are also shown. Dashed black lines indicate the plasmon energy and weight in an isolated graphene sheet. Overall, the QEH model is in excellent agreement with the full ab initio calculations performed for up to 3 layers of hBN.

structures.²¹ This shows that hybridization driven band structure effects, i.e., quantum confinement, have negligible influence on the dielectric properties of a vdWH which is the main reason for the success of the QEH model. The model result seems to converge toward the ab initio bulk result; however, convergence is not fully reached even for $N = 100$. The slow convergence toward the bulk result is mainly due to the spatial variation of the induced potential across the slab. In Figure 3c we show the z -dependent dielectric function defined as $\epsilon(z) = V_{\text{ext}}/V_{\text{tot}}(z)$, for a constant (along z) external potential with a long wavelength in-plane variation for $N = 50$. Although $\epsilon(z)$ is close to the ab initio bulk value (dashed line) in the middle of the slab, screening is strongly suppressed in the surface region. Increasing the slab thickness beyond 50 layers brings the QEH result even closer to the bulk result in the middle of the slab, but a small underestimation remains originating from the difference in the band structures of the monolayer and bulk systems. The suppressed screening in the surface region is a direct consequence of the anisotropic nature of the layered MoS₂ crystals, which limits the screening of perpendicular fields relative to in-plane fields, and is expected to be a general property of vdWHs.

The model can also be used to calculate the response to fields polarized along the z -direction, i.e., perpendicular to the layers. In this case the perpendicular component, $\epsilon_{zz}(\omega = 0)$,

can be calculated by applying an external potential with a linear variation along z . In the discrete basis of the QEH model, such a field is represented by a vector with 0 for all monopole components and 1 for all dipole components. Comparing the averaged slope of the total potential to the slope of the applied linear potential for a slab of $N = 100$ layers of MoS₂ yields $\epsilon_{zz} = 7.8$. This value is somewhat larger than the bulk value of 6.03; however, due to long-range surface effects the two numbers should not necessarily coincide. In fact, we find excellent agreement between the QEH model and full ab initio calculation of ϵ_{zz} for a four layer MoS₂ slab (see Supporting Information).

Next, we consider the hybridization of plasmons in graphene sheets separated by a hBN buffer layer of varying thickness, see Figure 4a. Plasmons in graphene on hBN were recently found to propagate with low loss,⁶ and the close to perfect lattice match between graphene and hBN enables full ab initio calculations for the thinnest heterostructures. Here we use doped graphene that has a finite density of states at the Fermi level, giving rise to metallic sheet plasmons with energies in the regime 0–2 eV. The plasmon energies go to zero in the optical limit, $q_{||} \rightarrow 0$, as characteristic for plasmons in 2D metals.^{22,23} We calculate the effect of hBN on the plasmons using the QEH model for up to 20 layers of hBN and compare to full ab initio calculations for 1–3 layers of hBN.

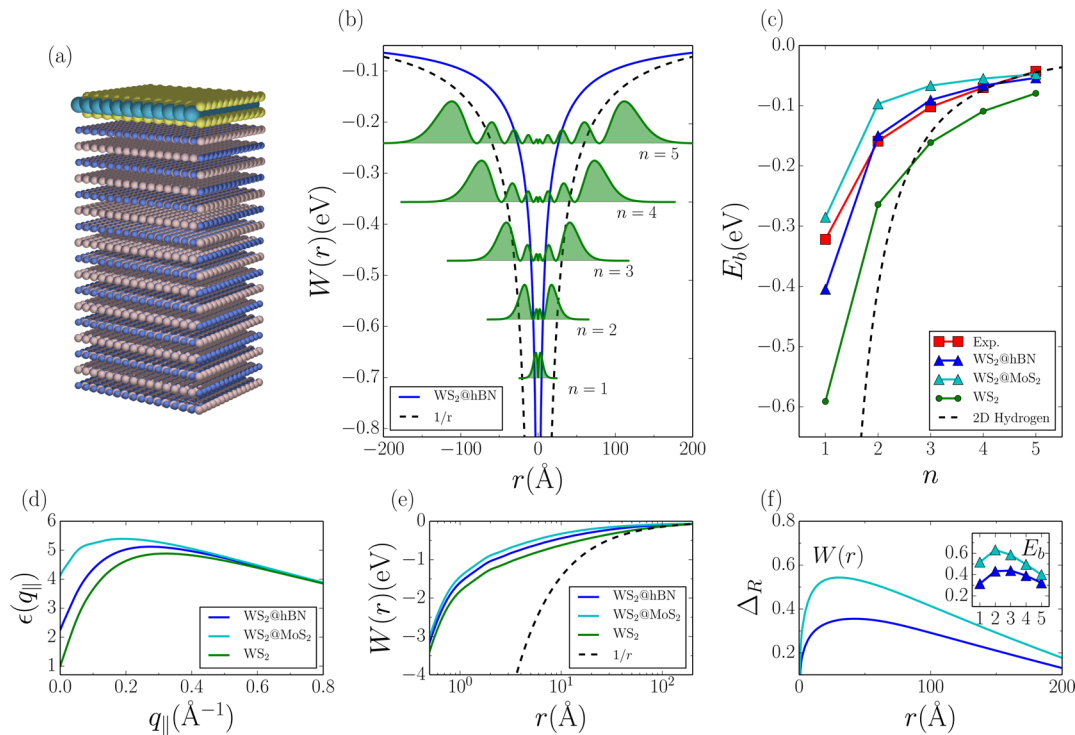


Figure 5. Excitons in supported WS₂. (a) Monolayer WS₂ adsorbed on a hBN substrate. (b) The screened interaction between an electron and a hole localized within a WS₂ monolayer adsorbed on hBN. For comparison the unscreened $1/r$ potential is shown. The radial probability distribution of the first five excitons, $r|F(r)|^2$, are also shown (arbitrary normalization). (c) The calculated binding energies of the lowest five excitons in freestanding WS₂ (green) and WS₂ on hBN (blue) and MoS₂ (cyan). Experimental values from ref 26 for WS₂ on SiO₂ are shown in red. The 2D hydrogen model with a $1/\epsilon r$ potential is shown for $\epsilon = 1.7$. (d) The dielectric function of the WS₂ layer defined as $\epsilon(q_{||}) = V(q_{||})/W(q_{||})$, where $V(q)$ and $W(q)$ are the bare and screened interaction in the WS₂ layer, respectively. (e) The screened interaction in the WS₂ layer as a function of $\log(r)$. (f) The relative difference between the screened interaction in the supported and freestanding WS₂. Inset shows the relative difference between E_b for the supported and freestanding WS₂.

To identify the plasmons of the heterostructure we follow ref 24. In brief, we compute the eigenvalues, $\epsilon_n(\omega)$, of the heterostructure dielectric function for each frequency point and identify a plasmon energy, $\hbar\omega_p$, from the condition $\text{Re}\epsilon_n(\omega_p) = 0$, see Figure 4b. The corresponding eigenvector, $\phi_n(\omega_p)$, represents the potential associated with the plasmon oscillation, see panel c. This analysis identifies two plasmons corresponding to the symmetric (++) and antisymmetric (+−) combinations of the graphene plasmons as previously found for two freestanding graphene sheets.²⁵ For 1–3 hBN layers, the QE model perfectly reproduces the ab initio results for the dielectric eigenvalues, plasmon energies, and weights. The weight is defined as the area under the peaks in the loss function $-\text{Im}\epsilon^{-1}(\mathbf{q}_{||}, \omega)$, see panel b. The densities and potentials of the plasmon eigenmodes shown in panel c are also reproduced fairly accurately by the model, where the qualitative differences for the induced densities, $\rho(z)$, are due to the use of a limited basis of the monopole and dipole response for each layer. In panels e and f the result of full ab initio calculations are shown by triangles, while the QE results are shown by continuous lines. The effect of the hBN buffer (dashed lines) is to red shift and dampen the plasmons compared to the result for two graphene sheets separated by the same amount of vacuum (full lines). This is also reflected by the relatively large amount of electron density located on the hBN during the plasma oscillation, see panel c.

Finally, we explore some characteristic features of excitons in freestanding and supported 2D semiconductors. A straightforward generalization of the well-known Mott–Wannier model²⁷

leads to the following eigenvalue equation for the excitons of a 2D semiconductor^{19,28}

$$\left[-\frac{\nabla_{2D}^2}{2\mu_{ex}} + W(\mathbf{r}) \right] F(\mathbf{r}) = E_b F(\mathbf{r}) \quad (7)$$

where E_b is the exciton binding energy, $F(\mathbf{r})$ is the wave function, μ_{ex} is the effective mass, and $W(\mathbf{r})$ is the screened electron–hole interaction. Assuming that the electron and hole are localized in layer 1, the Fourier transformed screened electron–hole interaction is obtained from the static ($\omega = 0$) response function (eq 4) and Coulomb interaction matrix (eq 5) of the QE model

$$W(\mathbf{q}_{||}) = V_{1M,1M}(\mathbf{q}_{||}) + \sum_{i\alpha,j\beta} V_{1M,j\beta}(\mathbf{q}_{||}) \chi_{j\beta,i\alpha}(\mathbf{q}_{||}) V_{i\alpha,1M}(\mathbf{q}_{||}) \quad (8)$$

The first term is the bare, i.e., unscreened, electron–hole interaction in layer 1 under the assumption that the electron and hole densities can be represented by the induced monopole density, $\rho_{1M}(z)$. The second term describes the screening from the surrounding layers and layer 1 itself. Note that the above equation can be easily generalized to describe the screened interaction between charges localized in different layers (relevant for indirect excitons).

In ref 26 Chernikov et al. observed a peculiar non-hydrogenic Rydberg series for the excitons in a single layer of WS₂ adsorbed on a SiO₂ substrate. Here we use the QE model to calculate the screened electron–hole interaction within the

WS₂ layer from the dielectric function of the full heterostructure. Since the QEH is applicable only to layered materials we place WS₂ on a 100 layer thick slab of hBN, which has dielectric constant very similar to that of SiO₂ (both around 4). For comparison we performed similar calculations using MoS₂ as substrate (dielectric constant larger than SiO₂). Figure 5c shows the five lowest *s*-excitons calculated from eq 7 for both freestanding and supported WS₂. For freestanding WS₂, we obtain $E_b = 0.59$ eV for the lowest exciton in good agreement with previous ab initio calculations.²⁹ The enhanced screening from the substrate lowers the exciton binding energies bringing the entire series closer to the experimental values (red), in particular for the hBN substrate.

The dielectric function of the WS₂ layer is defined as $\epsilon(q_{\parallel}) = V(q_{\parallel})/W(q_{\parallel})$, where $V(q_{\parallel})$ and $W(q_{\parallel})$ are the bare and screened interaction in the WS₂ layer, respectively. Figure 5d shows that the dielectric function of the supported WS₂ layer exceeds unity in the $q_{\parallel} \rightarrow 0$ limit. For structures of finite width, L , the dielectric function will in fact tend to unity for very small $q_{\parallel} \ll 1/L$. Here the results have been extrapolated to infinite substrate thickness, where $\epsilon(q_{\parallel})$ tends to a value larger than unity (in practice the extrapolation has no influence on the calculated exciton energies, i.e., they are well converged for $N = 100$). This means that the nature of the screening within the layer is not strictly 2D because the bulk substrate is able to screen the long wavelength fields. In real space, the screened potentials diverge as $\log(r)$ for small r and decay as $1/r$ for large r , see panel e. In panel f we show how the substrate affects $W(r)$: The relative deviation from $W(r)$ of the freestanding layer vanishes for small and large r but becomes significant at intermediate distances. As a consequence, the substrate-induced change in the exciton binding energy is relatively larger for intermediate exciton sizes. These results clearly demonstrate the profound, nonlocal influence of substrates on the dielectric screening and excitations in 2D materials.

In conclusion, we have demonstrated that the spatial and dynamical dielectric properties of a vdWH can be accurately and efficiently obtained from the dielectric properties of its constituent 2D crystals. The presented quantum-electrostatic heterostructure model (QEH) exploits this feature and enables the calculation of the dielectric properties and collective electronic excitations of realistic incommensurable heterostructures with ab initio precision. The dielectric building blocks for more than 50 different 2D materials are available in an open database allowing 2D materials researchers to efficiently predict and design the dielectric properties of realistic vdWHs.

■ ASSOCIATED CONTENT

Supporting Information

Detailed description of our quantum-electrostatic heterostructure (QEH) model and the computational details for all the ab initio calculations. The Supporting Information is available free of charge on the ACS Publications website at DOI: 10.1021/acs.nanolett.5b01251.

■ AUTHOR INFORMATION

Corresponding Authors

*E-mail: kiran@fysik.dtu.dk.

*E-mail: thygesen@fysik.dtu.dk.

Notes

The authors declare no competing financial interest.

■ ACKNOWLEDGMENTS

The authors thank Karsten Jacobsen for inspiring discussions. The authors acknowledge support from the Danish Council for Independent Research's Sapere Aude Program through grant no. 11-1051390. The Center for Nanostructured Graphene (CNG) is sponsored by the Danish National Research Foundation, Project DNRF58.

■ REFERENCES

- (1) Wang, Q. H.; Kalantar-Zadeh, K.; Kis, A.; Coleman, J. N.; Strano, M. S. *Nat. Nanotechnol.* **2012**, *7*, 699–712.
- (2) Şahin, H.; Cahangirov, S.; Topsakal, M.; Bekaroglu, E.; Akturk, E.; Senger, R. T.; Ciraci, S. *Phys. Rev. B* **2009**, *80*, 155453.
- (3) Britnell, L.; Ribeiro, R. M.; Eckmann, A.; Jalil, R.; Belle, B. D.; Mishchenko, A.; Kim, Y.-J.; Gorbachev, R. V.; Georgiou, T.; Morozov, S. V.; Grigorenko, A. N.; Geim, A. K.; Casiraghi, C.; Castro Neto, A. H.; Novoselov, K. S. *Science* **2013**, *340*, 1311–4.
- (4) Sup Choi, M.; Lee, G.-H.; Yu, Y.-J.; Lee, D.-Y.; Hwan Lee, S.; Kim, P.; Hone, J.; Jong Yoo, W. *Nat. Commun.* **2013**, *4*, 1624.
- (5) Shih, C. J.; Wang, Q. H.; Son, Y.; Jin, Z.; Blankschtein, D.; Strano, M. S. *ACS Nano* **2014**, *8*, 5790–5798.
- (6) Woessner, A.; Lundberg, M. B.; Gao, Y.; Principi, A.; Alonso-González, P.; Carrega, M.; Watanabe, K.; Taniguchi, T.; Vignale, G.; Polini, M.; Hone, J.; Hillenbrand, R.; Koppens, F. H. L. *Nat. Mater.* **2015**, *14*, 421–425.
- (7) Withers, F.; del Pozo-Zamudio, O.; Mishchenko, A.; Rooney, A. P.; Gholinia, A.; Watanabe, K.; Taniguchi, T.; Haigh, S. J.; Geim, A. K.; Tartakovsky, A. I.; Novoselov, K. S. *Nat. Mater.* **2015**, *14*, 301–306.
- (8) Geim, A. K.; Grigorieva, I. V. *Nature* **2013**, *499*, 419–25.
- (9) Woods, C. R.; et al. *Nat. Phys.* **2014**, *10*, 451–456.
- (10) Kang, J.; Li, J.; Li, S. S.; Xia, J. B.; Wang, L. W. *Nano Lett.* **2013**, *13*, 5485–5490.
- (11) Lu, C.-P.; Li, G.; Watanabe, K.; Taniguchi, T.; Andrei, E. *Phys. Rev. Lett.* **2014**, *113*, 156804.
- (12) Pitarke, J. M.; Silkin, V. M.; Chulkov, E. V.; Echenique, P. M. *Rep. Prog. Phys.* **2007**, *70*, 1–87.
- (13) Onida, G.; Reining, L.; Rubio, A. *Rev. Mod. Phys.* **2002**, *74*, 601–659.
- (14) Hybertsen, M. S.; Louie, S. G. *Phys. Rev. B* **1986**, *34*, 5390.
- (15) The dielectric building blocks and QEH software can be downloaded at <https://cmr.fysik.dtu.dk/vdwh/vdwh.html>.
- (16) Rasmussen, F. A.; Thygesen, K. S. *J. Phys. Chem. C* **2015**, DOI: 10.1021/acs.jpcc.5b02950.
- (17) Enkovaara, J.; et al. *J. Phys. Condens. Mater.* **2010**, *22*, 253202.
- (18) Yan, J.; Mortensen, J. J.; Jacobsen, K. W.; Thygesen, K. S. *Phys. Rev. B* **2011**, *83*, 245122.
- (19) Cudazzo, P.; Tokatly, I. V.; Rubio, A. *Phys. Rev. B* **2011**, *84*, 085406.
- (20) Hüser, F.; Olsen, T.; Thygesen, K. S. *Phys. Rev. B* **2013**, *87*, 1–14.
- (21) Cheiwchanchamnangij, T.; Lambrecht, W. R. L. *Phys. Rev. B* **2012**, *85*, 1–4.
- (22) Hwang, E.; Sarma, S. *Phys. Rev. B* **2007**, *75*, 205418.
- (23) Shin, S. Y.; Kim, N. D.; Kim, J. G.; Kim, K. S.; Noh, D. Y.; Kim, K. S.; Chung, J. W. *Appl. Phys. Lett.* **2011**, *99*, 082110.
- (24) Andersen, K.; Jacobsen, K. W.; Thygesen, K. S. *Phys. Rev. B* **2012**, *86*, 245129.
- (25) Hwang, E.; Das Sarma, S. *Phys. Rev. B* **2009**, *80*, 205405.
- (26) Chernikov, A.; Berkelbach, T. C.; Hill, H. M.; Rigosi, A.; Li, Y.; Aslan, O. B.; Reichman, D. R.; Hybertsen, M. S.; Heinz, T. F. *Phys. Rev. Lett.* **2014**, *113*, 076802.
- (27) Wannier, G. H. *Phys. Rev.* **1937**, *52*, 191.
- (28) Berkelbach, T. C.; Hybertsen, M. S.; Reichman, D. R. *Phys. Rev. B* **2013**, *88*, 045318.
- (29) Shi, H.; Pan, H.; Zhang, Y.-W.; Yakobson, B. I. *Phys. Rev. B* **2013**, *87*, 155304.